Earth and Planetary Science Letters 391 (2014) 137–145

Contents lists available at ScienceDirect

Earth and Planetary Science Letters

www.elsevier.com/locate/epsl

Reverberations, coda waves and ambient noise: Correlations at the global scale and retrieval of the deep phases

P. Boué [a,*], P. Poli [b], M. Campillo [a], P. Roux [a]

[a] Institut des Sciences de la Terre, Université Joseph Fourier and CNRS, Grenoble, France
[b] Department of Earth, Atmospheric and Planetary Sciences, Massachusetts Institute of Technology, Cambridge, MA, USA

ARTICLE INFO

Article history:
Received 8 November 2013
Received in revised form 29 January 2014
Accepted 30 January 2014
Available online 14 February 2014
Editor: P. Shearer

Keywords:
interferometry
body waves
global scale

ABSTRACT

Cross-correlation of continuous broadband records allows the retrieval of body waves at teleseismic distances. These continuous records mainly contain low-amplitude background noise that comes from ocean–crust interactions, although there are also many transient events of different magnitudes and their coda associated with reverberation and/or scattering. We present an analysis at the global scale of these different contributions in the context of body-wave retrieval using the cross-correlation technique. Specifically, we compare the correlation of long codas after strong earthquakes with those of the quietest days. In the long period range (25–100 s), several phases that propagate in the deep Earth are observed in the correlations of the signals recorded after earthquakes, with some of these phases showing non-physical polarization. At the same time, the global section of correlations shows a series of spurious branches. These features are reproduced with synthetic correlations. A stack of the quietest days of the year shows that body waves are still present, with relative amplitudes that are closer to those expected for the actual Earth response. When considering shorter periods (5–10 s), the reconstruction of the deep phases is not affected by the earthquake coda, due to the dominance of scattering over reverberation.

1. Introduction

From the regional to the global scale, ambient seismic noise primarily refers to the wavefield that is continuously produced by the interactions of the fluid envelopes, as mainly through ocean waves, and the solid Earth. The source mechanisms of these interactions are frequency dependent. Short-period noise (4 s to 30 s) is dominated by the two microseism peaks (e.g., Longuet-Higgins, 1950; Ardhuin et al., 2011). At longer periods (above 30 s), other mechanisms take place, which are also known as Earth hum (Kedar and Webb, 2005), such as the proposed shear-wave generation by infragravity waves (Fukao et al., 2010). Here the term "noise" is defined through its difference from the earthquake records. The duration of an earthquake record is defined with respect to a particular signal-to-noise ratio (SNR) threshold, and it varies with frequency for a given event magnitude. Furthermore, depending on the frequency, the scattering strength governs the ratio between the randomly scattered waves and the ballistic waves that reverberate between the main boundaries (i.e., the Earth surface, the core–mantle boundary).

It has been demonstrated that the elastic response between two stations can be evaluated by correlation of the records of scattered waves (Campillo and Paul, 2003) or long ambient noise records (Shapiro and Campillo, 2004). As expected from the theoretical Green's function between two points at the free surface, the correlations of continuous records are dominated by surface waves. The application of this approach has led to numerous examples of surface-wave imaging (e.g. Shapiro et al., 2005; Sabra et al., 2005a; Ritzwoller et al., 2011). The extension of the approach to body waves is indeed appealing, although the level of the remaining random fluctuations in the correlations makes the identification and exploitation of weak signals difficult. Furthermore, the sources of ambient noise are likely located at the surface, which results in a dominance of surface waves in the noise records. However, teleseismic body-waves have been observed in noise records (e.g. Vinnik, 1973; Gerstoft et al., 2008; Landès et al., 2010). The search for body waves in the correlations has been successful in the last few years, which started with the crustal phases (Zhan et al., 2010; Ruigrok et al., 2011; Poli et al., 2012a). Then, deep vertical reflections were detected from the mantle transition zone (Poli et al., 2012b) and from the core (Lin et al., 2013), with data from regional arrays. The complete teleseismic section was reconstructed by cross-correlation using a worldwide combination of arrays at short to long periods (5 s to 100 s; Boué et al., 2013) and at long to very long periods (30 s to

* Corresponding author. Tel.: +33 (0)4 76 63 52 39.
E-mail address: pierre.boue@ujf-grenoble.fr (P. Boué).

http://dx.doi.org/10.1016/j.epsl.2014.01.047
0012-821X/

300 s; Nishida, 2013). These last studies demonstrated the feasibility of ambient noise body-wave imaging. Lin and Tsai (2013) also discussed core-phase retrievals using antipodal station pairs.

Different processing has been used in all of these studies, and especially regarding the removal of transient signals. Nishida (2013) applied the most rigorous processing, using the Global Centroid Moment Tensor catalog (Ekström et al., 2012) to systematically remove long time windows corresponding to earthquakes and the following few days, the number of which depended on the event magnitude (Nishida and Kobayashi, 1999). Lin et al. (2013) and Boué et al. (2013) used less restrictive criteria. At the global scale, both Nishida (2013) and Boué et al. (2013) observed mantle body waves but obtained different results for the amplitudes of the core phases, which are weaker, and were more realistic in the correlation computed by Nishida (2013). Note that large-amplitude core phases were also reported by Lin et al. (2013).

Boué et al. (2013) questioned the relevance of these high-amplitude phases, and suggested that they show non-physical features. By non-physical, we mean here that these features do not appear in the natural Green's function. For example, the phase in the correlation corresponding to ScS is observed at short distances with strong amplitudes for the vertical component, which leads to an obvious problem of polarization. The presence of spurious arrivals in the correlation section challenges the applicability of noise imaging to body-wave problems in the deep Earth. We address this problem here, by analyzing the conditions under which reliable information can be extracted from noise correlations.

On the other hand, Lin et al. (2013) observed a strong correlation between the phases that reach the deepest parts of the Earth (ScS, P′P′df) and the seismicity. They suggested that earthquakes mainly excite these body waves. Finally the observations of Lin et al. (2013) and Boué et al. (2013) included spurious phases that are not in the Earth response, or at least, have different relative amplitudes. The problem of spurious arrivals due to multiples was discussed on a smaller scale by Snieder et al. (2006). Concerning wave propagation at the global scale, Ruigrok et al. (2008) discussed the imperfect reconstruction of the Green's function from surface source records, which reveals the presence of spurious arrivals (ghost events). They derived an elastodynamic relation from the representation theorem showing that knowledge of the responses of the medium with and without the effects of the free surface is required to retrieve the exact Green's function. They verified this theoretical statement numerically with acoustic simulations.

By investigating the temporal evolution of the reconstructed Green's function after large seismic events, it is shown in the present study that the processing used can explain these observations at long periods. The structure of this report is the following. First, the dataset used and the processing applied are shown. Then we compare the quality of the reconstruction of some of the phases with the seismicity and the microseism excitation over a whole year. We present a synthetic example of the reconstruction of the partial Green's functions using a simulated long time reverberated coda wavefield to explain the characteristics of spurious arrivals. Finally, the study focuses on the particular propagation geometry between Finland and Japan.

2. Data and processing

In this study, one year was selected (2008) for the vertical-component records from a set of 420 stations distributed worldwide (Fig. 1). The BH channels are used after removal of the instrumental response, and decimation to a 5-Hz sampling frequency. Note that some of these stations are not available during the whole of the year period. All of the networks involved are detailed in Appendix A. The continuous records were processed similarly to

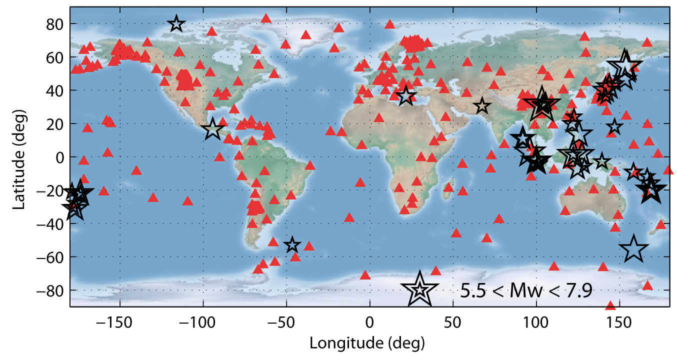

Fig. 1. Map of the network used in this study (see Appendix A for details). Triangles, location of the 420 seismic stations; stars, earthquakes (Mw > 5.5) that corresponds to HCDs.

Boué et al. (2013), which includes spectral normalization of the noise traces (whitening). Cross-correlations are computed for 4-h time windows, with a correlation lag of 4000 s, and normalized through the square root of the energy of both of the traces. They are directly stacked over one day, in the 5 s to 100 s period band. With this processing, we can detect and choose to remove the 4-h time window that contain ballistic arrivals of strong transient events (Boué et al., 2013). At the same time, the scattered and reverberated coda waves from earthquakes are retained. Eventually, the dataset contained more than 80 000 correlations per day, which corresponds to each possible station pair. These correlations can then be stacked either over a given period (e.g., days, weeks), which results in one correlation per station pair, or over space, which results to one correlation for a given average distance (bin) per day. The combination of both stacks corresponds to the global section, for which correlations are sorted as a function of distance from 0° to 180° with a bin size of 0.1°, and stacked over the year. This is shown in Fig. 2b, as the resulting vertical–vertical correlations, which represent the global average propagation. It is therefore justified to compare this with the synthetic Green's function computed in a spherical Earth using the Preliminary Reference Earth Model (Dziewonski and Anderson, 1981). Fig. 2a shows the synthetic seismograms computed using the spectral element method (Nissen-Meyer et al. 2007, 2008). We simulate a simple vertical point force with a Gaussian-shaped dominant period of 40 s. Although we note a general visual agreement that indicates that numerous deep phases are emerging from the correlation, there are some noticeable discrepancies, some of which have non-physical characteristics. The comparison between Fig. 2a and 2b should remain qualitative, as the 3D Earth structure favors the emergence of some phases after the spatial stack on the real data section (Fig. 2b). For example, Rayleigh waves can stack destructively, particularly at short periods, due to heterogeneities in shallow structures of the Earth.

In the global correlation section, some arrivals are present before the direct P-wave (Fig. 2b). As already noted, the ScS phase has too high relative amplitude. Even if the section representation with correlations stacked over distance bins enhances small move-out phases with a more constructive stack compared to large move-out phases like Rayleigh waves, it remains that ScS should not be visible on a vertical-component section at a distance close to 0°. Other deep phases, such as PKP and P′P′df, have high amplitudes relatively to the mantle, or even to the Rayleigh wave. Finally, there are some low-frequency spurious arrivals between the ScS and the P′P′df. In the following, we study how reverberated waves that follow large earthquakes affect the correlations. As the daily correlation for a given pair does not show a sufficient SNR, it is necessary to stack the correlations over space to produce

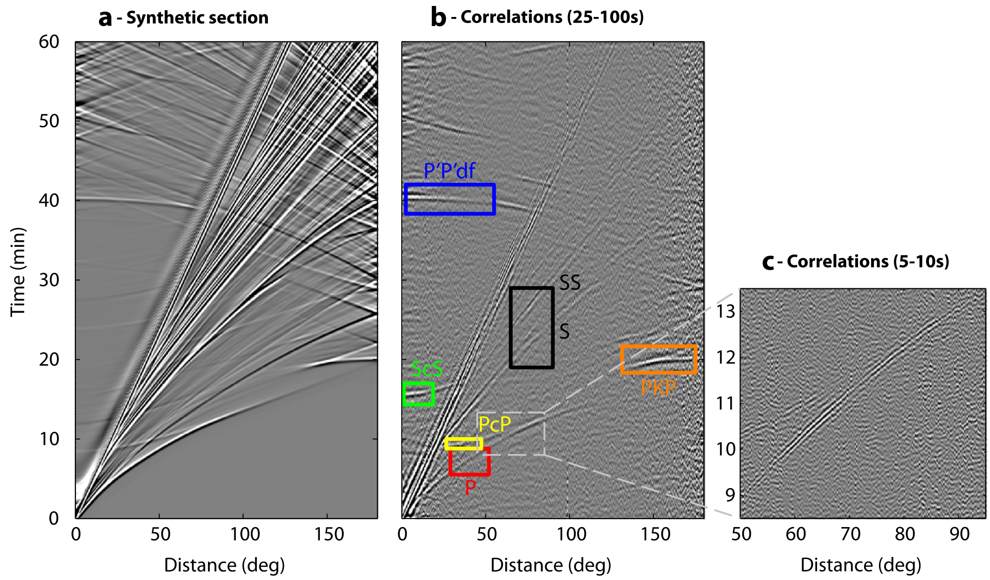

Fig. 2. (a) Synthetic Green's function in the PREM model with a dominant period of 40 s. (b) Correlations stack over the whole year, filtered in 25 s to 100 s period bands, and sorted as functions of inter-station distance with a bin size of 0.1°. Color boxes, area used for the 2D correlations over each day: P (red), PcP (yellow), ScS (green), PKP (orange), S and SS (black) and P′P′df (blue). (c) Detail of the P-PcP waves in the 5-s to 10-s period band. (For interpretation of the references to colour in this figure legend, the reader is referred to the web version of this article.)

the daily reconstructed signals. In practice we consider bins of 0.1° for the spatial average.

3. Contributions to correlations

We construct daily global sections that are used to evaluate the temporal evolution of the contributions of the daily correlations to the reconstructed Green's function. The daily contributions are quantified by computing the coherence between the daily and yearly reconstructions in specific time–distance domains. We selected six different time–space domains that correspond to different phases (Fig. 2b, colored boxes), and processed the image correlation for the 366 days of the year. This processing was performed with sections that had been filtered in the short period (5–10 s) and long period (25–100 s) ranges. The data are shown in Fig. 3. High coherence means strong excitation of the given phase for a given day. These coherences are compared to the daily seismicity (Fig. 3a) and oceanic secondary microseism excitation (Fig. 3b) from Hillers et al. (2012). The daily cumulative seismic moment is computed from the International Seimological Centre catalog after the selection of events with a magnitude >4. Ocean excitation for the secondary microseism includes bathymetric effects (Longuet-Higgins, 1950), and this is integrated over the whole ocean surface.

At short period, P and PcP are well reconstructed, as shown in Fig. 2c. The daily coherence of these two phases (Fig. 3c) is independent of the seismicity rate. This indicates the efficiency of the initial processing that included the removal of large earthquakes for this period range. There is also no clear relationship between the time-dependent coherence of the reconstructed waves and the amplitude of the secondary microseism excitation, even if this excitation varies by two orders of magnitude. This indicates that after the normalization of the correlations, their properties are independent of the amplitude of the ocean excitation, which is probably due to its complex spatial and temporal source pattern. Globally, the coherence appears stationary through the year. We interpret this point as the signature of the inherently complex nature of the short-period ambient noise with a significant contribution of scattered waves.

A different picture is drawn from the results for long-period correlations. The main feature shown in Fig. 3d is the strong correlation of the main deep phases with seismicity. In the 25-s to 100-s period band, the main deep phases, such as ScS and P′P′df, and also PcP and PKP, are strongly correlated to seismicity. This is shown by the high amplitude peaks of the daily coherence for the large earthquakes, as also highlighted by the gray vertical lines in Fig. 3d. A similar observation was made by Lin et al. (2013) and Lin and Tsai (2013) for regional and antipodal propagations respectively. For the mantle P-waves and S-waves, no such strong correlation with seismicity is observed. However a correlation is observed for a series of events in February. These high-coherence peaks are not coincident with the strong maxima of the core phases. Some smaller peaks for the S-SS phases are not correlated with any strong earthquakes, as for example in May or November. This suggests another source contribution for these S-waves at long periods, which might be associated with the coupling of ocean infragravity waves with the seabed topography, as proposed by Fukao et al. (2010). Furthermore, some coherence peaks are extended to the days after the earthquake. This illustrates the importance of the long-standing reverberations following large magnitude events. Note that even in the case of the largest event in the year 2008, the May 12 Mw 7.9 Sichuan earthquake, the high coherence period does not exceed 2 days after the mainshock.

The value of the coherence is difficult to analyze, as it depends on the source–receiver geometry, focal mechanism, and receiver–receiver geometry. We observe that large earthquakes do not always lead to high coherence peaks. The correlation with seismicity is nevertheless obvious for deep phases. In the following, we isolate the contributions of earthquakes to the global correlations, and we analyze their part in the emergence of spurious arrivals or anomalous polarizations. This will lead to modified processing for long-period correlations.

4. Long-period processing

Using the long-period band, the coherence is presented in Fig. 3d, where we define high-coherence days (HCDs) by selecting the days with high seismic activity that are also associated with high coherence for each phase. In practice, we selected days with a coherence >0.2 and with a corresponding local maximum in the cumulative seismic moment function. For the mantle P-waves and S-waves, this results in selecting a group of days that corre-

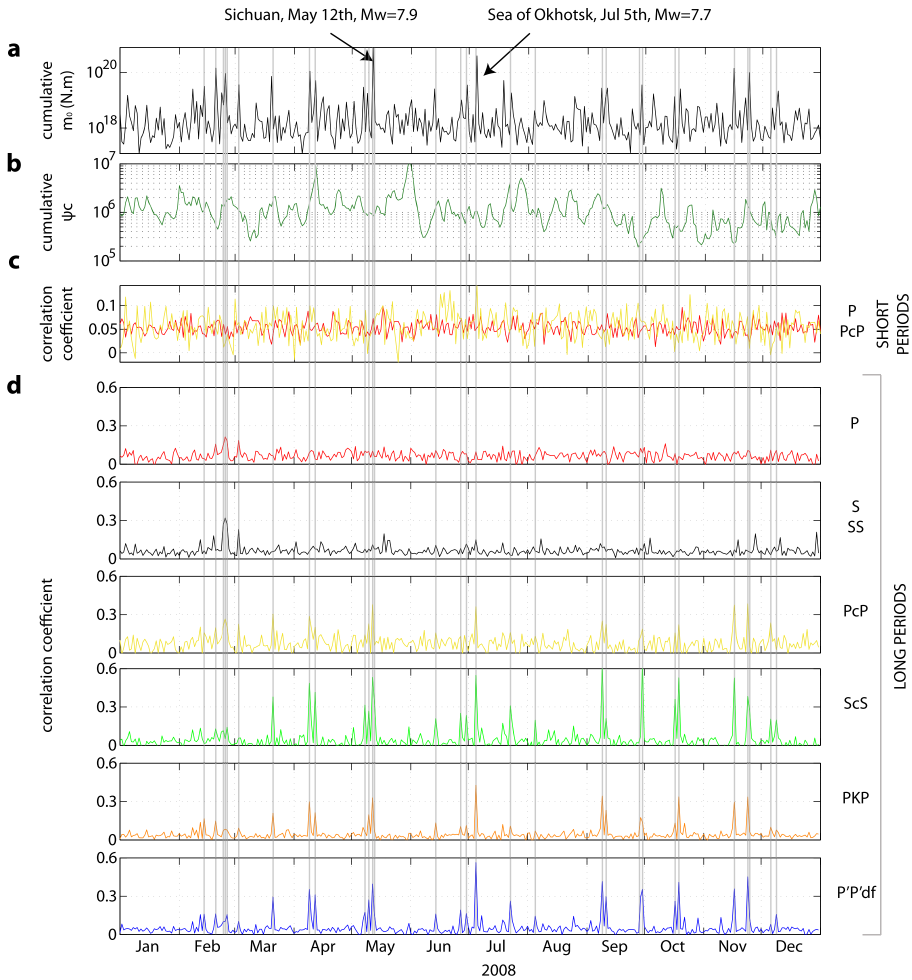

Fig. 3. (a) Daily cumulative seismic moment (m_0) for the year 2008. (b) Cumulative microseim excitation at 7 s from ocean wave–wave interactions modulated by bathymetry (global summation). (c) Two-dimensional correlation of the daily P (red) and PcP (yellow) waves at the short period. (d) Two-dimensional correlations of the daily global section with the year-stacked global section at the long period and for the different phases. Vertical gray lines, the HCDs. (For interpretation of the references to colour in this figure legend, the reader is referred to the web version of this article.)

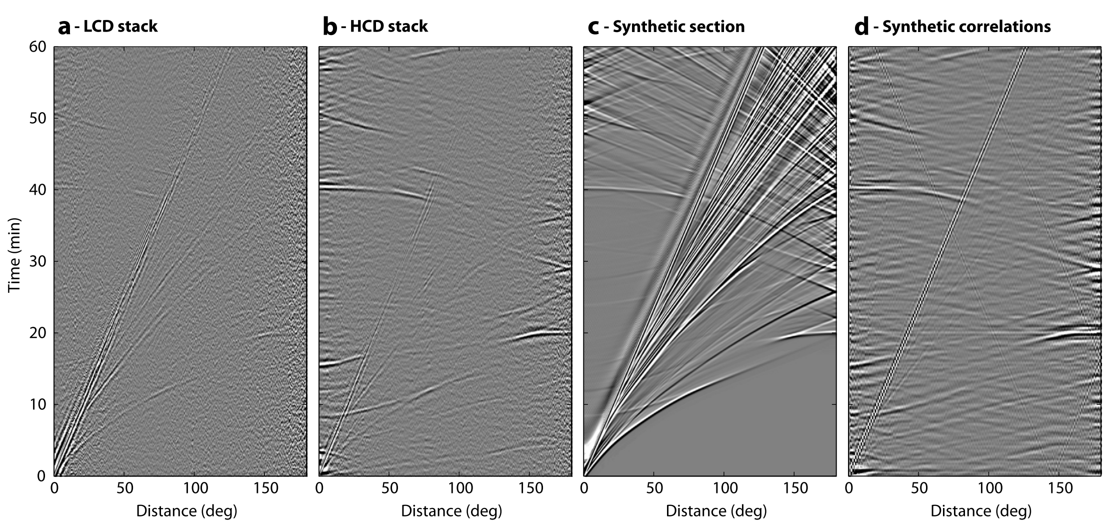

Fig. 4. (a) Global section stacked for the 336 LCDs of the year, and (b) for the 30 HCDs (Fig. 3, vertical lines). (c) Synthetic section from a 40-s dominant period vertical source in a spherical Earth, using PREM. (d) Cross-correlation of a 2-day-long synthetic coda in the same model.

spond to the high-amplitude peaks in February and March. For the deep reflected waves, a criterion based on the average fluctuations of the coherence is used to detect the local maxima. In the end, 30 days are considered as HCDs. The remaining days of the year are considered as low-coherence days (LCDs). We now compare the teleseismic correlation sections built from these subsets.

Correlations that correspond to LCD and HCD subsets are stacked, to get two global sections; these sections are shown in Fig. 4a and b, respectively. A comparison of these two sections shows that the spurious phases that are visible on the global section of Fig. 2b are related to the HCDs, and thus to the strong seismic activity. Fig. 4a (for the LCDs) shows a lower SNR than the year stack (Fig. 2b), although no spurious arrivals are visible and the relative amplitudes of the different phases fit the theoretical Green's function better, which is also shown in Fig. 4c. The section for LCDs is close to the data of Nishida (2013), but here only for a 336-day stack.

On the other hand, spurious arrivals (as previously described) are illustrated in Fig. 4b. With the relatively low amplitude of the Rayleigh wave, there is a spurious arrival with a negative move-out between 0° and 20° and for times <5 min. Spurious phases arrive ahead of the P-wave. This HCD section also shows abnormally high relative amplitudes for phases, such as for ScS, PKP and P′P′df. The previous observations suggested that the HCD section is dominated by correlation cross-terms between the various reverberated waves that continue for tens of hours after a large earthquake. This is a variant of the process of emergence of spurious arrivals that was described by Snieder et al. (2006).

The anomalous amplitudes appear for phases with very small move-out (i.e., very large apparent velocity). In the absence of a significant scattering at long periods, we postulate that the strong contributions for the reflections in the correlations are generated by multiple reflections. These multiple deep reflections have large Fresnel zones, which means that the region in which a source contributes is also very large. A source that is not along an eigenray joining the two stations, but in a wide Fresnel zone, nevertheless has a contribution. This can result in incorrect delays in the arrival times, and also potentially in polarization anomalies. To test this hypothesis, a synthetic example of a global scale cross-correlation was computed. This experiment simulates the contributions of impulsive sources to the correlations. A vertical point force is applied at the surface of a spherical model (PREM) which includes attenuation. The wavefield is computed for a propagation duration of 2 days and recorded at numerous positions at the Earth surface. As the problem is axis symmetric, the computation can be restricted to receiver points on a great circle. We apply the same cross-correlation processing to the 2-day-long synthetics as for the real data. The resulting correlations are sorted by distance between the sensors and are stacked for all available source positions. Using the reciprocity theorem, this simulation is equivalent to having sources everywhere on the Earth surface and to the computing of the resulting cross-correlation for any sensor combination. The synthetic section is shown in Fig. 4d. The main phases of the Earth Green's function are reconstructed. The anomalous characteristics that have been observed in the HCD section (Fig. 4b) are visible: strong amplitudes of deep reflected waves with flat move-out, a spurious arrival before the P-wave arrival-time, and the inverse move-out phase in the range 0–20° and 0–5 min. This excellent qualitative agreement shows that anomalous phases in the correlations are produced by the coherent impulsive earthquake sources. This analysis was carried out for a global distribution of sources and stations. To go further in the understanding of the retrieved body waves at the global scale, we have to focus on a specific geometry; i.e., a specific travel path, to evaluate the impact of localized sources.

5. A specific geometry: the FNET–LAPNET dataset

The FNET (Japan) and LAPNET (Finland) arrays were selected (Fig. 5, blue triangles), as they are both dense (*ca*. 40 stations) and with relatively small apertures compare to their relative distance (*ca*. 63°). We first repeat the processing of the selection of HCDs and LCDs for this selected dataset. The comparisons between correlations stacked for the whole year for the HCDs and the LCDs are shown in Fig. 6. Specifically, we focus on S, SS and P′P′df waves at long period (Fig. 6a–c), and on the P and PcP waves at short period (Fig. 6d–f). The mantle P-wave at the long period is too weak to be visible on this section representation. Fig. 6b shows that P′P′df is dominant for HCDs. Also, we can see lower amplitude flat move-out spurious arrivals due to correlation cross-terms from multiple reverberations. The Rayleigh wave, and also the S and SS waves are reconstructed in the stacking of the LCD. At shorter period, Fig. 3 shows that the P and PcP waves in the noise correlations are not associated with coherent contributions of earthquakes. These two waves are well retrieved in the LCD stack. Fig. 6 shows the theoretical arrival times for PREM (Fig. 6, red lines), which confirm the phase identifications and indicate qualitative agreement even for the P′P′df phase, with an anomalous amplitude relatively to other phases at long periods.

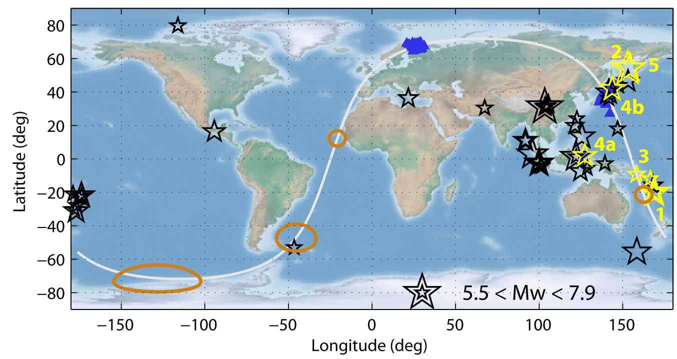

Fig. 5. Map of the two dense arrays: LAPNET (Finland) and FNET (Japan). Blue triangles, positions of the stations; white line, great circle that crosses these two arrays; orange patches, two first endfire lobes (two bounces) for the mantle P-wave at 7-s for these two arrays; stars, earthquakes (Mw > 5.5) that correspond to the HCDs; yellow stars, as related to Fig. 8. (For interpretation of the references to colour in this figure, the reader is referred to the web version of this article.)

To analyze the time accuracy of the different reconstructed phases, we performed slant stacks based on the theoretical travel-time curves (PREM). These data are presented in Fig. 7, where the travel-time obtained for all of the year, the HCD stack and the LCD stack are compared. At short period, there is no significant phase shift between the stacks for the P (Fig. 7a) and PcP (Fig. 7b) phases. The LCD stack gives a better SNR than the HCD stack, with a much stronger emergence of the signal. The SNR is expected to be directly related to the square root of the duration of the time series, which have been correlated (Sabra et al., 2005c; Larose et al., 2008). Here, this effect accounts for a factor about 3.5 in favor of the LCD. This is similar to our observations. This indicates that there is no specific effect of reverberated short-period waves after a few hours following an earthquake. This supports the pertinence of the processing, and the origin of the correlations in the waves continuously generated by the oceanic gravity waves, especially in the frequency bandwidth corresponding to secondary microseisms.

At longer period, the S-wave (Fig. 6c) is only visible on the LCD. The SS-wave (Fig. 7d) does not emerge from the slant stack, even if it appears to be visible in Fig. 6. Finally, the P′P′df phase (Fig. 7e) is visible on both the LCDs and HCDs, with a better SNR on the HCD stack, as seen in Fig. 6. The two waveforms, both of which are filtered in the 25–100 s period band, show different dominant periods according to their corresponding sources. The HCD trace is dominated by longer period waves, coming from earthquakes, than those of the LCD trace. We measured a significant time shift at a 50 s central period, of about 4.5 s. This difference can suggest a shift associated with unevenly distributed noise sources at the Earth surface, similar to the 2D effect discussed in 2D by Froment et al. (2010).

To study the potential effects associated with source geometry, we reproduced the coherence analysis of Fig. 3 but limiting the

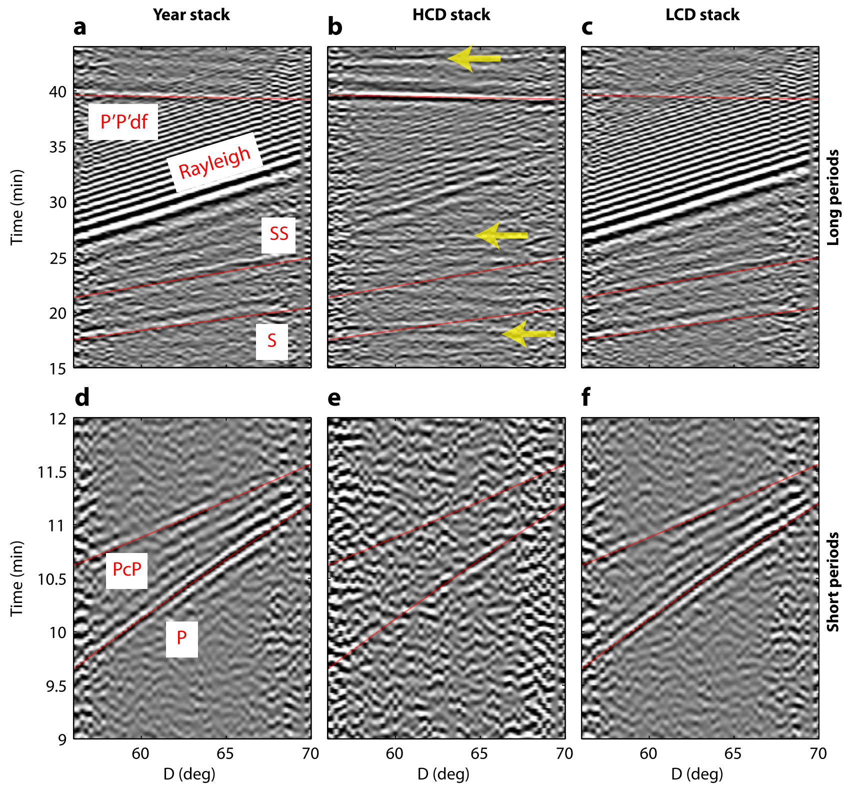

Fig. 6. Correlation between LAPNET and FNET arrays sorted as a function of distance. (a–c) At long period. (d–f) At short period. Red lines, theoretical travel-times using PREM. (a, d) Year stack; (b, e) HCDs; (c, f) LCDs. Yellow arrows indicate some spurious phases in the HCD stack. (For interpretation of the references to colour in this figure legend, the reader is referred to the web version of this article.)

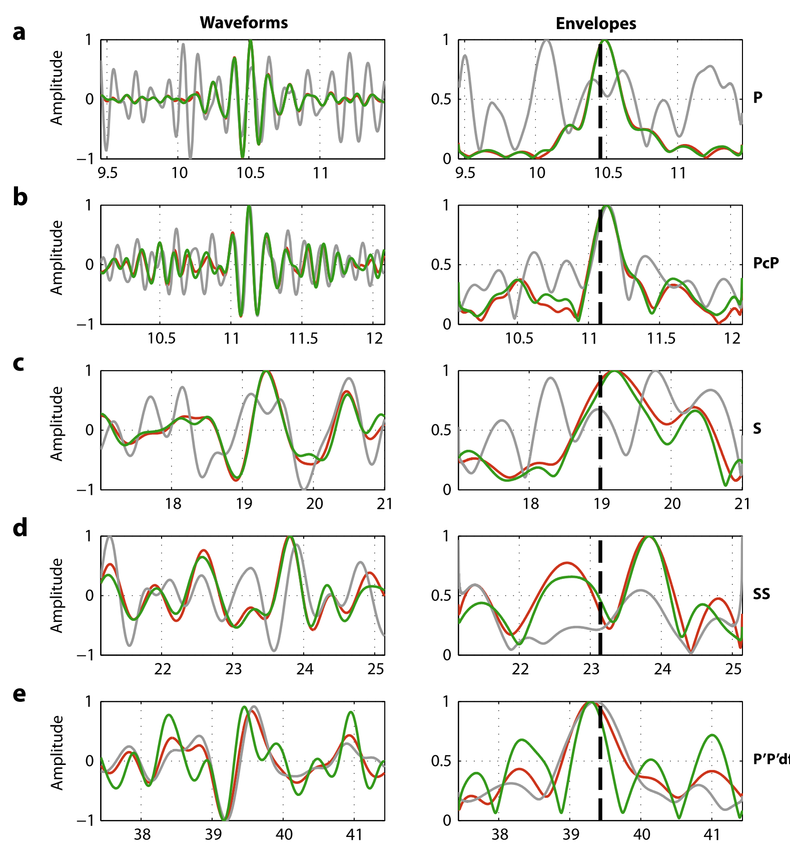

Fig. 7. Correlation stacks using theoretical arrival times from PREM and between FNET and LAPNET. Red line, the year stack; gray line, the HCD stack; green line, the LCD stack. Vertical dashed lines, theoretical arrival time for each phase (PREM). Left panels show the waveforms. Right panels show the corresponding envelopes. (a) Short period P. (b) Short period PcP. (c) Long period S. (d) Long period SS. (e) Long period P′P′df. (For interpretation of the references to colour in this figure legend, the reader is referred to the web version of this article.)

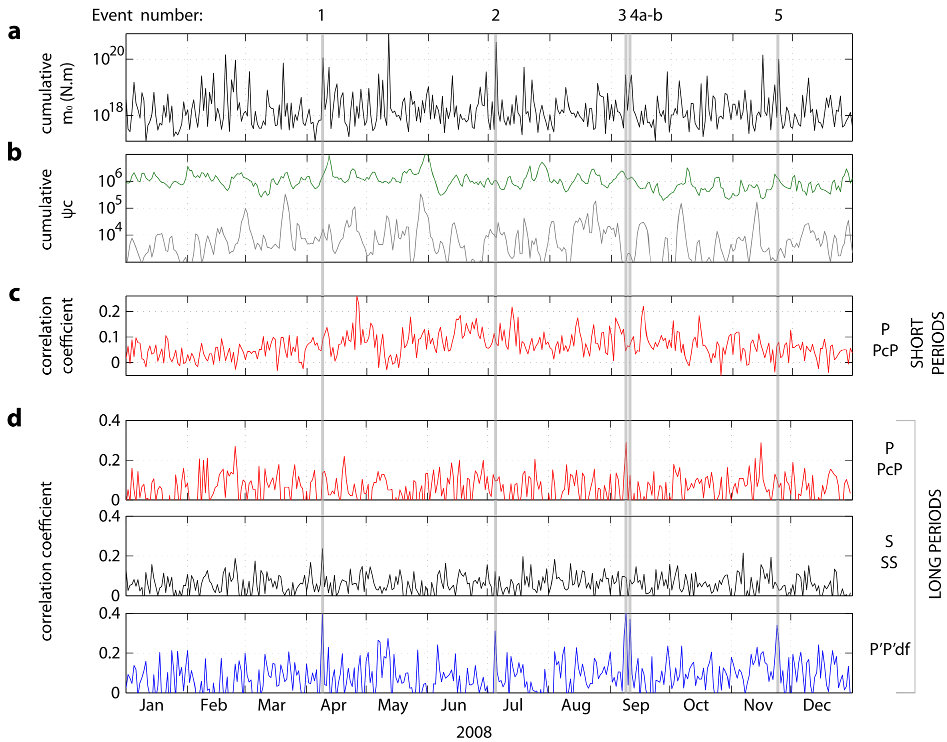

Fig. 8. (a) Daily cumulative seismic moment (m_0) for the year 2008. (b) Daily cumulative microseim excitation at 7 s from the ocean wave–wave interaction modulate by bathymetry. Green, global summation; gray, summation limited to P-wave endfire areas. (c) Two-dimensional correlation of daily P-PcP waves at the short period. (d) Two-dimensional correlations of daily global section with the year-stacked global section at the long period and for different phases. Vertical gray lines, HCDs that remain for this dataset. (For interpretation of the references to colour in this figure legend, the reader is referred to the web version of this article.)

analysis to the FNET to LAPNET paths. The results are presented in Fig. 8. Daily cumulative seismic moment and secondary microseism excitation from the ocean are also reported for comparison.

At shorter period, there is still no clear correlation between phase coherence and seismic activity or microseism excitation. To be more specific, we evaluated the microseism in the region where it is expected to contribute coherently to the correlations. We define these geographical areas (lobes) as the Fresnel zones on the Earth surface of the first two bounces of the P-waves (Fig. 5). These so-called endfire lobes were described by Sabra et al. (2005b) for an oceanic waveguide. On the assumption of a radial velocity model (no lateral heterogeneities), all of these lobes are located along the great circle joining the two arrays, and their radius increases for each successive bounce. Even with this processing, there is no observation of any clear relationship between microseism excitation and specific event in the daily coherence series. The exact origin of the short period signals observed remains unclear. Nevertheless, this can indicate that the coherence is probably more controlled by the large-scale spatial distribution of the sources than by the amplitude of specific events, as expected for the contribution of scattered waves. This is illustrated in Fig. 8c, where there is a slight seasonal trend with higher amplitude during the northern hemisphere summer. This might be related to the location of the endfire lobes, as mainly in the southern hemisphere, where the excitation is dominant during the northern hemisphere summer (Landès et al., 2010).

At long periods, the effect of scattering as large as for the short period is not expected. We have shown also the importance of the long-standing multiple reflections, that we refer to as reverberations. For the long period range, Fig. 8d shows a smaller number of coherence peaks than in Fig. 3, for the entire set of station-to-station paths. This indicates a selective geometrical effect. The main coherence peaks observed for the FNET–LAPNET paths are still correlated to seismic activity. This is particularly true for the

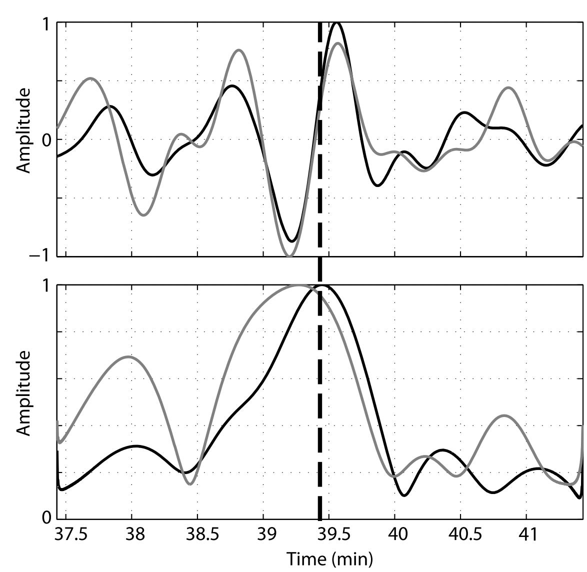

Fig. 9. Comparison between the P′P′df phases reconstructed the day of events 1 (black) and 2 (gray). Top panel: waveforms; bottom panel: corresponding envelopes; vertical dashed line, theoretical arrival time given by PREM.

P′P′df phase. Mantle P-waves and S-waves do not show such strong correlations with seismicity. The P′P′df phase, which has the larger coherence peaks, is used to define the set of days that were associated with strong contributions to the correlations. The epicenters of the large events that occurred on these days are shown in Fig. 5 (yellow stars). Note the absence among these events of the largest earthquake of the year, namely the May 8, 2008, Sichuan earthquake. A group of events is located along the great circle that joins the centers of the networks (Fig. 5, white). Event 4a shown in Fig. 5 is located far from the great circle, but we cannot distinguish its influence with respect to event 4b, which occurred the same day and was located on the great circle. Events 2 and 5 (Fig. 5) were selected, although they do not belong to the great circle. These last events are deep earthquakes (>500 km), and they produced a coherence peak only for P′P′df.

Finally, the time accuracy of the P′P′df phase is evaluated at long period as a function of the location of sources for HCDs. Fig. 9 shows the slant stack of P′P′df for all of the correlations of the two arrays, but only for the days corresponding to events 1 and 2, respectively. Even if both of these waveforms show similar shapes, their envelopes reveal a clearly different arrival-time. The P′P′df phase that was reconstructed from event 2 (out of the great circle between the two array centers), arrived several seconds before the PREM theoretical time. This is not the case for event 1, which was aligned with the two arrays, and so might better contribute to the Green's reconstruction. Phase shift analysis reveals a 2 s delay at a 50 s central period. Even if this time delay is smaller than that observed using envelopes, this is a good indication that the use of correlations of multiple reflections from large earthquakes should be used with caution for travel-time measurements.

6. Conclusions

Nishida (2013) and Boué et al. (2013) showed that the global scale propagation of body waves can be retrieved by cross-correlation of continuous records. The conditions of the reconstruction of the deep body phases are different for the period band considered here. Two elements are to be considered: the nature of the excitation, and the part of the scattering associated to wave propagation.

The relation between seismicity and deep phase reconstructions at long period (25–100 s) is illustrated here on the global scale, as it was performed at short distances by Lin et al. (2013) and for antipodal station pairs by Lin and Tsai (2013). This is particularly clear for core reflected and transmitted phases, but not very clear for P and S mantle phases. Also, these reconstructed signals show amplitude and polarization anomalies. We reproduced the main spurious patterns with synthetic seismograms and their correlations. These spurious arrivals correspond to correlations between various coherent phases that are generated by earthquakes, although they are not strictly part of the physical Green's function. These discrepancies are theoretically expected from the analysis of the reconstruction of the Green's function based on the representation theorem proposed by Ruigrok et al. (2008). With the removal of the coherent earthquake wavefield from the dataset, which can last several days for large events, we obtain correlations of ambient noise that are closer to the theoretical Green's function and exempt of spurious phases. At shorter period (5–10 s), the reconstructed phases are not correlated with seismicity, which is probably due to the prominence of scattering over reverberation. No clear correlation was found between the phase reconstruction and the microseism excitation amplitude. This is what we would expect as the effect of the correlation processing combined with the nature of the source excitation, which is a spatially extended uncorrelated continuous source. The difference in the behavior between scattered short-period waves and reverberated long-period waves is explained because the scattering enhanced the directional diversity of the waves. Ideally, the correlation of scattered waves leads to the exact Green's function (Campillo and Paul, 2003). In contrast, in spite of their long duration, the long-period reverberations locally conserve a narrow directionality. These behaviors were formulated mathematically by Garnier and Papanicolaou (2009, 2012). At long periods, with the scattering being weaker, the effect on the correlations is not expected to be as strong as at short periods.

Finally, a particular receiver geometry was chosen (LAPNET–FNET) to study the effects of the source location with respect to the areas of constructive contributions. The earthquakes that contribute to high daily coherence are mainly aligned with station-to-station direction. Nevertheless, an example of a clear travel-time bias on the P′P′df phase is shown for a single event with high coherence. Particular care has therefore to be taken at the long period to remove long coherent reverberated waves, for the recovery of the natural Earth elastic response with useful accuracy.

Table 1
List of seimic networks used in this study. The descriptions are from IRIS metadata aggregator.

Identifier	Description	Stations selected (n)
AI	Antarctic Seismographic Argentinean Italian Network	3
AK	Alaska Regional Network	30
BO	Bosai-Ken Network (FNET, NIED)	40
CN	Canadian National Seismograph Network	13
CU	Caribbean Network (USGS)	8
G	GEOSCOPE	21
GE	GEOFON	20
GT	Global Telemetered Seismograph Network (USAF/USGS)	6
IC	New China Digital Seismograph Network	9
II	Global Seismograph Network (GSN-IRIS/IDA)	34
IU	Global Seismograph Network (GSN-IRIS/USGS)	60
MN	MEDNET Project	12
PS	Pacific21	6
TA	USArray Transportable Array (NSF EarthScope Project)	42
TW	Broadband Array in Taiwan for Seismology	7
X4	ASCENT	30
XK	LAPNET	41
ZL	Sierras Pampeanas	37

Acknowledgements

This study was supported by the European Research Council through the advanced grant Whisper 227507. All of the data used in this study were obtained through the IRIS, NIED and RESIF data centers. We used data from numerous seismic networks, and we thank all of the dedicated seismologists and technical staff who run these networks for making their seismic data available. Finally the authors thank Kees Wapenaar and an anonymous reviewer for their careful review and constructive comments that helped in improving this manuscript.

Appendix A

Table 1 shows the different networks used for the present study, with a brief description and the number of station actually selected. Except for the FNET and LAPNET data, all of the waveforms were downloaded using PYTHON request protocols: obspy.iris and obspy.arclink packages.

References

Ardhuin, F., Stutzmann, E., Schimmel, M., Mangeney, A., 2011. Ocean wave sources of seismic noise. J. Geophys. Res., Oceans, (ISSN 2156-2202) 116 (C9). http://dx.doi.org/10.1029/2011JC006952.

Boué, P., Poli, P., Campillo, M., Pedersen, H., Briand, X., Roux, P., 2013. Teleseismic correlations of ambient seismic noise for deep global imaging of the earth. Geophys. J. Int. 194 (2), 844–848. http://dx.doi.org/10.1093/gji/ggt160.

Campillo, M., Paul, A., 2003. Long-range correlations in the diffuse seismic coda. Science 299 (5606), 547–549. http://dx.doi.org/10.1126/science.1078551.

Dziewonski, A.M., Anderson, D.L., 1981. Preliminary reference earth model. Phys. Earth Planet. Inter., (ISSN 0031-9201) 25 (4), 297–356. http://dx.doi.org/10.1016/0031-9201(81)90046-7.

Ekström, G., Nettles, M., Dziewoński, A., 2012. The global CMT project 2004–2010: Centroid-moment tensors for 13,017 earthquakes. Phys. Earth Planet. Inter., (ISSN 0031-9201) 200–201 (1), 1–9. http://dx.doi.org/10.1016/j.pepi.2012.04.002.

Froment, B., Campillo, M., Roux, P., Gouédard, P., Verdel, A., Weaver, R.L., 2010. Estimation of the effect of nonisotropically distributed energy on the apparent arrival time in correlations. Geophysics 75 (5), SA85–SA93. http://dx.doi.org/10.1190/1.3483102.
Fukao, Y., Nishida, K., Kobayashi, N., 2010. Seafloor topography, ocean infragravity waves, and background love and Rayleigh waves. J. Geophys. Res. Solid Earth, (ISSN 2156-2202) 115 (B4). http://dx.doi.org/10.1029/2009JB006678.
Garnier, J., Papanicolaou, G., 2009. Passive sensor imaging using cross correlations of noisy signals in a scattering medium. SIAM J. Imaging Sci. 2 (2), 396–437. http://dx.doi.org/10.1137/080723454.
Garnier, J., Papanicolaou, G., 2012. Correlation-based virtual source imaging in strongly scattering random media. Inverse Probl. 28 (7), 075002.
Gerstoft, P., Shearer, P.M., Harmon, N., Zhang, J., 2008. Global p, pp, and pkp wave microseisms observed from distant storms. Geophys. Res. Lett., (ISSN 1944-8007) 35 (23). http://dx.doi.org/10.1029/2008GL036111.
Hillers, G., Graham, N., Campillo, M., Kedar, S., Landès, M., Shapiro, N., 2012. Global oceanic microseism sources as seen by seismic arrays and predicted by wave action models. Geochem. Geophys. Geosyst. 13, Q01021. http://dx.doi.org/10.1029/2011GC003875.
Kedar, S., Webb, F.H., 2005. The ocean's seismic hum. Science 307 (5710), 682–683. http://dx.doi.org/10.1126/science.1108380.
Landès, M., Hubans, F., Shapiro, N.M., Paul, A., Campillo, M., 2010. Origin of deep ocean microseisms by using teleseismic body waves. J. Geophys. Res. Solid Earth, (ISSN 2156-2202) 115 (B5), B05302. http://dx.doi.org/10.1029/2009JB006918.
Larose, E., Roux, P., Campillo, M., Derode, A., 2008. Fluctuations of correlations and Green's function reconstruction: Role of scattering. J. Appl. Phys. 103 (11), 114907. http://dx.doi.org/10.1063/1.2939267.
Lin, F.-C., Tsai, V.C., 2013. Seismic interferometry with antipodal station pairs. Geophys. Res. Lett., (ISSN 1944-8007) 40 (17), 4609–4613. http://dx.doi.org/10.1002/grl.50907.
Lin, F.-C., Tsai, V.C., Schmandt, B., Duputel, Z., Zhan, Z., 2013. Extracting seismic core phases with array interferometry. Geophys. Res. Lett., (ISSN 1944-8007) 40 (6), 1049–1053. http://dx.doi.org/10.1002/grl.50237.
Longuet-Higgins, M.S., 1950. A theory of the origin of microseisms. Philos. Trans. R. Soc. Lond. Ser. A, Math. Phys. Sci. 243 (857), 1–35. http://dx.doi.org/10.1098/rsta.1950.0012.
Nishida, K., 2013. Global propagation of body waves revealed by cross-correlation analysis of seismic hum. Geophys. Res. Lett., (ISSN 1944-8007), 1–6. http://dx.doi.org/10.1002/grl.50269.
Nishida, K., Kobayashi, N., 1999. Statistical features of Earth's continuous free oscillations. J. Geophys. Res. Solid Earth, (ISSN 2156-2202) 104 (B12), 28741–28750. http://dx.doi.org/10.1029/1999JB900286.
Nissen-Meyer, T., Fournier, A., Dahlen, F., 2007. A two-dimensional spectral-element method for computing spherical-earth seismograms. 1. Moment-tensor source. Geophys. J. Int. 168 (3), 1067–1092. http://dx.doi.org/10.1111/j.1365-246X.2006.03121.x.
Nissen-Meyer, T., Fournier, A., Dahlen, F.A., 2008. A 2-d spectral-element method for computing spherical-earth seismograms. 2. Waves in solid-fluid media. Geophys. J. Int. 174 (3), 873–888. http://dx.doi.org/10.1111/j.1365-246X.2008.03813.x.
Poli, P., Pedersen, H.A., Campillo, M., 2012a. Emergence of body waves from cross-correlation of short period seismic noise. Geophys. J. Int. 188 (2), 549–558. http://dx.doi.org/10.1111/j.1365-246X.2011.05271.x.
Poli, P., Campillo, M., Pedersen, H., Group, L.W., 2012b. Body-wave imaging of Earth's mantle discontinuities from ambient seismic noise. Science 338 (6110), 1063–1065. http://dx.doi.org/10.1126/science.1228194.
Ritzwoller, M.H., Lin, F.-C., Shen, W., 2011. Ambient noise tomography with a large seismic array. C. R. Géosci. 343, 558–570. http://dx.doi.org/10.1016/j.crte.2011.03.007.
Ruigrok, E., Draganov, D., Wapenaar, K., 2008. Global-scale seismic interferometry: theory and numerical examples. Geophys. Prospect. 56, 395–417. http://dx.doi.org/10.1111/j.1365-2478.2008.00697.
Ruigrok, E., Campman, X., Wapenaar, K., 2011. Extraction of p-wave reflections from microseisms. C. R. Géosci. 343, 512–525. http://dx.doi.org/10.1016/j.crte.2011.02.006.
Sabra, K.G., Gerstoft, P., Roux, P., Kuperman, W.A., Fehler, M.C., 2005a. Surface wave tomography from microseisms in Southern California. Geophys. Res. Lett. 32 (14). http://dx.doi.org/10.1029/2005GL023155.
Sabra, K.G., Roux, P., Kuperman, W.A., 2005b. Arrival-time structure of the time-averaged ambient noise cross-correlation function in an oceanic waveguide. J. Acoust. Soc. Am. 117 (1), 164–174. http://dx.doi.org/10.1121/1.1835507.
Sabra, K.G., Roux, P., Kuperman, W.A., 2005c. Emergence rate of the time-domain, Green's function from the ambient noise cross-correlation function. J. Acoust. Soc. Am. 118 (6), 3524–3531. http://dx.doi.org/10.1121/1.2109059.
Shapiro, N.M., Campillo, M., 2004. Emergence of broadband Rayleigh waves from correlations of the ambient seismic noise. Geophys. Res. Lett. 31, L07614. http://dx.doi.org/10.1029/2004GL019491.
Shapiro, N.M., Campillo, M., Stehly, L., Ritzwoller, M., 2005. High-resolution surface-wave tomography from ambient seismic noise. Science 307 (5715), 1615–1618. http://dx.doi.org/10.1126/science.1108339.
Snieder, R., Wapenaar, K., Larner, K., 2006. Spurious multiples in seismic interferometry of primaries. Geophysics 71 (4), SI111–SI124. http://dx.doi.org/10.1190/1.2211507.
Vinnik, L., 1973. Sources of microseismic p waves. Pure Appl. Geophys., (ISSN 0033-4553) 103 (1), 282–289. http://dx.doi.org/10.1007/BF00876404.
Zhan, Z., Ni, S., Helmberger, D.V., Clayton, R.W., 2010. Retrieval of moho-reflected shear wave arrivals from ambient seismic noise. Geophys. J. Int., (ISSN 1365-246X) 182 (1), 408–420. http://dx.doi.org/10.1111/j.1365-246X.2010.04625.x.